Contract No. and Disclaimer:

Tuning of Size and Shape of Au-Pt Nanocatalyst for Direct Methanol Fuel Cells

Simona E. Hunyadi Murph,[1]* Catherine J. Murphy,[2] Hector R.Colon-Mercado,[1] Ricardo D. Torres,[1] Katie J. Heroux,[1] Elise B. Fox,[1] Lucas B. Thompson,[2] Richard T. Haasch[3]

[1]*Savannah River National Laboratory, Savannah River Site, 735-11A, Aiken, SC 29808*
[2] *Department of Chemistry, University of Illinois at Urbana-Champaign, 600 S. Mathews Ave, Urbana, IL 61801*
[3]*Frederick Seitz Materials Research Laboratory, University of Illinois at Urbana-Champaign, 302 MRL, MC-230, Urbana, IL 61801*

**To whom correspondence should be addressed*
*Simona.Murph@srnl.doe.gov , Phone #: 1-803-725-8159, Fax: 1-803-725-4478

Abstract
In this paper, we report the precise control of the size, shape and surface morphology of Au-Pt nanocatalysts (cubes, blocks, octahedrons and dogbones) synthesized via a seed-mediated approach. Gold 'seeds' of different aspect ratios (1 to 4.2), grown by a silver-assisted approach, were used as templates for high-yield production of novel Au-Pt nanocatalysts at a low temperature (40 ^{o}C). Characterization by electron microscopy (SEM, TEM, HRTEM), energy dispersive X-ray analysis (EDX), UV-Vis spectroscopy, zeta-potential (surface charge), atomic force microscopy (AFM), X-ray photoelectron spectroscopy (XPS) and inductively coupled plasma mass spectrometry (ICP-MS) were used to better understand their physico-chemical properties, preferred reactivities and underlying nanoparticle growth mechanism. A rotating disk electrode was used to evaluate the Au-Pt nanocatalysts electrochemical performance in the oxygen reduction reaction (ORR) and the methanol oxidation reaction (MOR) of direct methanol fuel cells. The results indicate the Au-Pt dogbones are partially and in some cases completely unaffected by methanol poisoning during the evaluation of the ORR. The ORR performance of the octahedron particles in the absence of MeOH is superior to that of the Au-Pt dogbones and Pt-black, however its performance is affected by the presence of MeOH.

Keywords: gold-platinum nanocatalysts, direct methanol fuel cells, anisotropic nanostructures

CTAB: cetyltrimethylammonium bromide

MOR: methanol oxidation reaction

ORR: oxygen reduction reaction

Introduction

Fuel cells have been studied and developed extensively as one of the most feasible option for alternative energy vehicles and portable power applications. Direct methanol fuel cells (DMFCs) are particularly attractive as potential alternatives to conventional batteries due to their high efficiency, high power density, low pollution, and longevity (Hunyadi Murph et al. 2010, 2011; McNicol et al. 1999; Zhong et al. 2010). DMFC applications are wide-ranging, from automobiles and space vehicles to electronic devices such as computers and cellular phones. Although platinum (Pt) and Pt-containing catalysts have proven to be the most efficient for DMFC applications, the high precious metal load requirements must be overcome for large commercialization to be viable (Antolini et al. 2008; Zhong et al. 2010). To minimize Pt content while still enhancing DMFC efficiencies, much research has been devoted to Pt nanostructures that maximize surface area to volume ratios (Chen et al. 2010; Tian et al. 2007; Xia et al. 2009; Zhong et al. 2010). The larger surface area provides a higher density of active sites, leading to more efficient utilization of the platinum and enhanced kinetics of catalysis.

Recent studies have shown that bimetallic nanoparticles often show enhanced stability and catalytic selectivity when compared to the parent metals (He et al. 2010; Park et al 2008; Ren et al. 2010; Somorjai et al 2005; Zeng et al. 2006). The presence of a shell metal on the core lattice can affect the original crystal structure and thus the electronic and optical properties of the material (Hunyadi Murph et al. 2011, Ortiz-Soto et al. 2006). For example, several groups have reported that the Au-Pt interface of bimetallic nanocatalysts effectively suppresses CO adsorption onto the Pt active surface (Ren et al. 2010; Zeng et al. 2006). Carbon monoxide (CO) is an intermediate product during DMFC operation, which forms due to the slow kinetics of the methanol oxidation reaction (MOR) at the anode (McNicol et al. 1999; Zhong et al. 2010; Hunyadi Murph et al. 2011). CO poisons the Pt nanocatalysts, significantly reducing DMFC efficiency by slowing down the highly irreversible MOR and the oxygen reduction reaction (ORR) at the cathode (Roucoux et al. 2002; Williams et al. 1997; Bell 2003; Chen et al. 1997; Paulus et al 2000; Bell 2003; Liang et al. 2004). The presence of Au in bimetallic nanocatalysts has shown to alter the Pt electronic band structure leading to a synergistic catalytic effect, which modifies the strength for oxygen surface adsorption in the ORR (Zhong et al. 2010). Other studies (Zhang et al. 2007) have also demonstrated that Au nanoclusters can stabilize the Pt nanocatalysts in the ORR against dissolution (Pt^{2+} formation) under potential electrocycling regimes (a continuous problem in fuel cells for vehicle applications).

Limited reports have examined the catalytic behavior of anisotropic bimetallic Au-Pt nanoparticles with controllable shape, size and composition. The development of novel bimetallic nanostructures with monodisperse size and shape has been hindered by the lack of facile and reproducible synthesis protocols. This area of research is of particular interest for catalytic applications, as anisotropic nanomaterials can display distinct properties and functionalities along their different crystal facets (Tian et al. 2007; Xia et al. 2009; Vidal-Iglesias et al. 2004, Somorjai and Blakely 1975). The crystal shape dictates its surface atomic arrangement, which is directly related to the material's catalytic activity and stability (Burda et al. 2005; Narayanan et al. 2003; Narayanan et al. 2005a, b; Zecchina et al. 2007). As atoms at the crystal edges and corners have more uncoordinated sites, they are likely to be more reactive (Hunyadi Murph et al. 2011; Xia et al. 2009).

Reports by Guo et al. (2007, 2008) examined the catalytic activity of hybrid Au-Pt nanorods and size-controllable urchin-like Au-Pt nanoparticles for the electrochemical reduction of oxygen. They found that these novel structures exhibited higher catalytic activities than Pt nanoparticles of similar size due to the higher surface-to-volume ratios and Pt utilization efficiency. A more recent study also reported on Au-Pt nanorods grown in situ into thermosensitive core-shell microgel particles, which also showed highly enhanced catalytic activity for the reduction of 4-nitrophenol due to the synergistic effect of the bimetallic structure (Lu et al. 2010). Wang et al. (2008) also observed improved formic acid electrooxidation with Au-Pt nanorods relative to conventional Pt/C catalysts. While these results are highly promising, additional studies should be conducted to fundamentally understand the shape-morphology-porosity-dependence of these anisotropic nanoparticles on their catalytic activity. To understand this relationship, a facile and systematic synthesis protocol should be developed which maximizes the active surface, edge, and corner sites of these Au-Pt nanocatalysts. Extensive characterization of these variable aspect ratio structures will provide valuable information on how their atomic arrangement and preferred morphologies affect their catalytic behavior, particularly in fuel cell reactions.

In this paper, we report the precise control of the size, shape and surface morphology of Au-Pt nanocatalysts produced by systematic variation of the initial dimensions of Au nanoparticle templates and the Ag^+ ion concentration utilized in the experimental method. Au nanoparticle templates or 'seeds' with different morphologies (shapes and sizes) were produced by a silver-assisted growth procedure, as reported earlier (Murphy et al. 2005). A hetereopitaxial solution-based approach was subsequently used to produce a variety of novel Au-Pt nanostructures, including cubes, blocks, octahedrons, and dogbones. The high-yield synthesis is done at a mild temperature (40^oC) in the presence of the seed templates, Pt ions, an aqueous surfactant (cetyltrimethylammonium bromide, CTAB) and a mild reducing agent (ascorbic acid). The electrochemical performance of these nanocatalysts for potential fuel cell applications, particularly the oxygen reduction reaction (ORR) and the methanol oxidation reaction (MOR), was evaluated in a rotating disk electrode.

Experimental procedure

Materials: Chloroauric acid trihydrate ($HAuCl_4 \cdot 3H_2O$), trisodium citrate ($Na_3C_6H_5O_7$), sodium borohydride ($NaBH_4$), ascorbic acid ($C_6H_8O_6$), silver nitrate ($AgNO_3$), potassium tetrachloro-platinate (II) (K_2PtCl_4) and cetyltrimethylammonium bromide (CTAB) were purchased from Sigma Aldrich. All chemicals were used as received. All glassware was cleaned with aqua regia (HCl:HNO3, 3:1) and thoroughly rinsed with deionized water prior use.

Synthesis of Au nanoparticle seeds: Gold nanoparticles, including spheres and rods of aspect ratios (length/width) ranging from 1 to 4.2 were prepared by a silver-mediated surfactant approach, as described in our previous reports (Sau et al. 2004; Hunyadi Murph et al. 2010, 2011; Murphy et al. 2005, 2006). In this method, gold nucleation centers (1.5-2 nm) are initially synthesized for further metal overgrowth. A solution of 2.5×10^{-4} M $HAuCl_4$ was initially prepared in 0.1 M CTAB and 600 μL of $NaBH_4$ (10mM) were subsequently added at 0°C while vigorously stirring for 2 min. The resulting gold nucleation centers were used in the synthesis of the gold templates for the Au-Pt nanocatalysts. In this method,the following aqueous solutions were added to a conical flask: 9.5 mL of 0.1 M CTAB solution, varying amounts of 5 mM silver nitrate (10, 40, 80, 160 or 200 uL, depending on the resulting aspect ratio) and 0.5 mL of 10 mM chloroauric acid. Subsequently, 55 uL of 0.1 M ascorbic acid was then added followed by 12 uL gold nucleation center solution. The resulting nanoparticle templates were left undisturbed for 4-6 hours until further use.

Synthesis of Au-Pt nanocatalysts: The Au nanoparticle seeds were used as templates for Pt overgrowth. Bimetallic nanoparticles of various shapes and aspect ratios were prepared by adding 5mL of as-prepared and unpurified Au nanoparticle seeds to a growth solution containing 0.05mM K_2PtCl_4 and 0.1M CTAB. 16 uL of 1M ascorbic acid were subsequently added to this dispersion and stirred for 10 hours at 40^oC. Excess surfactant was removed by two successive centrifugation and re-dispersion steps in DI water.

Electrochemical studies: A Pine Instruments Rotating Ring Disk Electrode (RDE) provided data on the kinetics of the reaction at the cathode. 60 µL of the nanoparticles suspenion in DI H_2O were drop-casted (30 µL at the time) onto the glassy carbon (5 mm diameter disc) surface and dried at 35 ºC under vacuum (typical drying time 40 min.).. The catalyst was then coated with 4 µL of a 1/20 5 wt% Nafion/ethanol solution. A dispersion of commercial platinum black (HiSPEC^{TM} 1000) was also tested as a comparison. Platinum black (1mg/mL of solution) was dispersed and 10 µL were deposited on the glassy carbon surface. The RDE current output during the potential sweep was used to determine the electrode reactions in 0.5 M H_2SO_4 and in a 0.5 M H_2SO_4 /0.1 M MeOH solution. A graphite counter electrode and a double junction Ag/AgCl reference electrode were used. Cyclic voltammograms were collected under an Ar blanket at 50 mV/s and 10 mV/s. The solution was then saturated with O_2 and linear sweep measurements were recorded from 0-1200 rpm (in increments of 200 rpm) at 10 mV/s. All potentials were normalized to the standard hydrogen electrode (SHE). All electrochemical measurements were taken using a bipotentiostat (Model AFCBP1 from Pine Instruments).

Instrumentation: UV-vis spectroscopy was performed with Varian model Cary 500 Scan UV-Vis-NIR spectrophotometer. Light scattering and ξ-potential measurements were performed with a Brookhaven Zeta PALS instrument. Low-resolution transmission electron microscope (TEM) images were acquired with a 200kV Hitachi H-8000 instrument. High-resolution TEM images and energy dispersive spectra (EDX) were acquired with a 200kV JEOL 2100F microscope equipped with a CEOS GmbH hexapole probe corrector. TEM samples were prepared by drop-casting the purified nanoparticle solution (10 uL) on holey-carbon Cu grids and allowing them to dry at

ambient conditions. Photoelectron spectra of the Au-Pt nanoparticles were acquired on a Kratos Axis Ultra XPS spectrometer using a monochromatic Kα x-ray source with 40 eV pass energy. The resulting spectra were energy corrected to the Au 4f peak binding energy of 84 eV. XPS substrates were prepared by depositing a concentrated solution of Au-Pt rods on a silicon wafer previously washed with piranha solution (H_2SO_4:H2O2, 3:1). The substrate was then dried in an oven at 70 °C. Atomic force microscopy (AFM) height measurements of drop-casted nanoparticles were collected with either of two scanning probe microscopes (Veeco Digital Instruments): (i) a Multimode SPM operated with a Nanoscope III controller, or (ii) a CP-II SPM equipped with an Autoprobe Electronic Module (AEM) controller. The microscopes were operated in tapping mode with cantilever tips with a nominal radius of 8 nm (P-doped Si, Model RTESP, Veeco Digital Instruments).

Results and Discussions

Characterization of Au nanoparticle seeds of varied aspect ratios (AR=Length/Width):

The synthesis of the Au nanoparticle seeds used for Pt overgrowth was carried out via a two step silver-assisted wet chemical approach (Sau et al. 2004; Murphy et al. 2005; Murphy et al. 2006; Hunyadi Murph et al. 2010, 2011). In our experiments, different Ag^+ ion concentrations were investigated as a way to control the shape, size and aspect ratio of the resulting Au seed template. Table 1 and Figure 1 shows that small changes of the Ag^+ ion concentrations in the reaction procedure, from $0.5x10^{-5}$ M to $10.0x10^{-5}$ M, resulted in either spherical or rod-like Au nanoparticles of different dimensions. A small amount of Ag^+ ions produces spherical nanostructures with a diameter of 28±2 nm while increasing amounts results in elongated structures of lengths ranging from 47±3 to 76±3 nm with diameters ~20 nm. Transmission electron microscopy (TEM) images (Figure 1) shows good size and shape uniformity of the Au nanoparticle seeds with aspect ratios ranging from 1 to 4.2. Throughout the manuscript we will refer to the above Au nanoparticles as Au 1, Au 2, Au 3, Au 4, and Au 5.

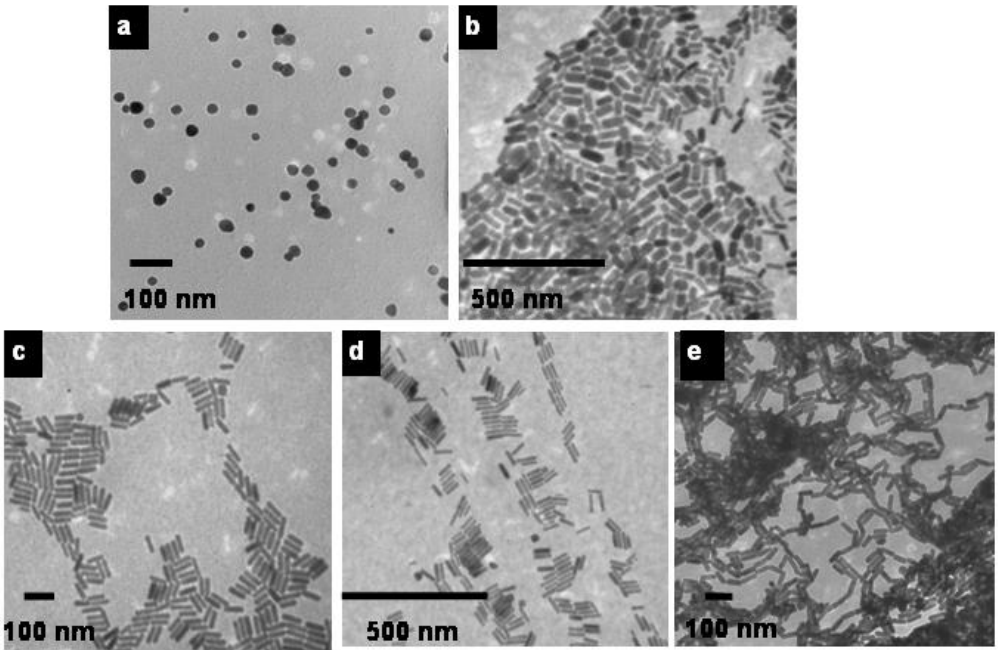

Figure 1. TEM images of Au seed nanoparticles of increasing aspect ratio prepared by a silver assisted approach: (a) 1, (b) 2.1, (c) 3.1, (d) 3.3, (e) 4.2. Scale bar: 100 nm –a, c, and e, 500 nm- b and d.

Table 1. Dimensional characteristics of Au nanoparticle seeds and resulting Au-Pt nanocatalysts. Each product nanocatalyst is listed under the starting seed template.

Sample	Nominal [Ag+], $x10^{-5}$ M	Dimensions		Aspect Ratio (AR), L/W	Morphology	Percent Yield, %
		Length (L), nm	Width (W), nm			
Au 1	0.5	28±2	28±2	1	spheres	94
Au-Pt 1		42±1	47±1	1.1	octahedrons	90
Au 2a	2	47±3	23±1	2.1	rods	87
Au 2b	2	36±2	36±2	1	spheres	13
Au-Pt 2a		42±2	32±2	1.2	cubes	12
Au-Pt 2b		53±3	32±2	1.7	blocks	83
Au 3	6	64±2	20±2	3.1	rods	95
Au-Pt 3		70±2	24±2	2.9	dogbones	94
Au 4	8	71±2	21±2	3.3	rods	96
Au-Pt 4		75±3	24±2	3.1	dogbones	95
Au 5	10	76±3	19±2	4.2	rods	96
Au-Pt 5		83±3	24±2	3.5	dogbones	95

High resolution TEM (HRTEM) was used to characterize the lattice arrangement and crystallinity of the Au nanoparticle seeds. HRTEM images of the nanospheres (Au 2a) and the nanorods (Au 3) display well-defined, continuous and equally-spaced fringe patterns for their atomic lattice (Figure 2). The Au nanospheres continuous fringes support their single-crystallinity. Previous reports have concluded that single-crystal seeds are obtained when CTAB is used during borohydride reduction of $HAuCl_4$ (Liu et al. 2005). The high yields of single-crystalline nanospheres and nanorods have made this by far the most popular synthetic procedure.

Guyot-Sionnest et al. have reported on the critical role of the Ag^+ ions in the growth mechanism of Au nanorods from single-crystal seeds (Liu et al. 2005). In the presence of Ag^+ ions, single-crystal nanorods grow along the [100] with side {110} and {100} facets. These results agreed with the classical growth description based on Au nanorods electrochemically synthesized (Wang et al. 1999; Yu et al. 1997). El Sayed's group elucidated a crystal structure with an octagonal cross-section, bound by alternate {100} and {110} facets, which coverge at the tips in the form of {110} and {111} facets, respectively. Further HRTEM studies suggested that the less stable {110} surfaces could exist due to CTAB stabilization (Wang et al. 2000). However, missing row reconstructions could be observed at defect sites where the capping micelle molecules are missing.

Recent studies have argued that the assesment by El-Sayed's group does not necessarily hold valid for Au nanorods synthesized by a seeded synthetic method. Using particles synthesized by the silver-assisted approach, Liz-Marzan's group performed HRTEM on Au nanorods standing perpendicular to the substrate (Carbo-Argibay et al. 2010). Their analysis provided evidence that the <100> and <110> crystallographic directions point toward lateral edges, and thus the faces joining on them must be assigned to eight-identical higher index {250} facets. A more recent study used electron tomography and thickness profile measurements to determine the three-dimensional shape of single-crystal Au nanorods, also synthesized by a silver-assisted and seed-mediated approach (Katz-Boon, et al. 2011). The authors provide evidence that the nanorod octagonal side facets are sparsely packed atomic planes, all belonging to the same symmetry-equivalent family {0 5 12}. The rods endcaps have a pyramidal shape made up of slightly different facets, which connect to the rod by four small {0 5 12} facets. These results indicate that further experiments are needed to conclusively resolve this dispute and correctly identity the exposed crystallographic facets of these Au nanorods.

Figure 2b displays a synthesized Au nanorod seed (Au 3) laying flat on the carbon film of a TEM grid. The particle displays continuous {002} fringes ($d \sim 0.204$ nm) which might indicate that the electron beam was aligned in the [001] direction. As expected, the absence of stacking faults, twins or volume dislocations suggests that the Au nanorods prepared by our silver-assisted seed mediated approach produces single-crystal structures. The corresponding electron diffraction

pattern (Figure 2b insert) displays high symmetry of the face-centered cubic lattice. Preliminary analysis of the pattern shows a spot array with regular spacings and uniform angles between the planes, which further supports the single-crystal assessment of the seeds. More rigorous indexing studies are underway to further understand the preferred growth facets of these colloids and shed some more light on the ongoing debate.

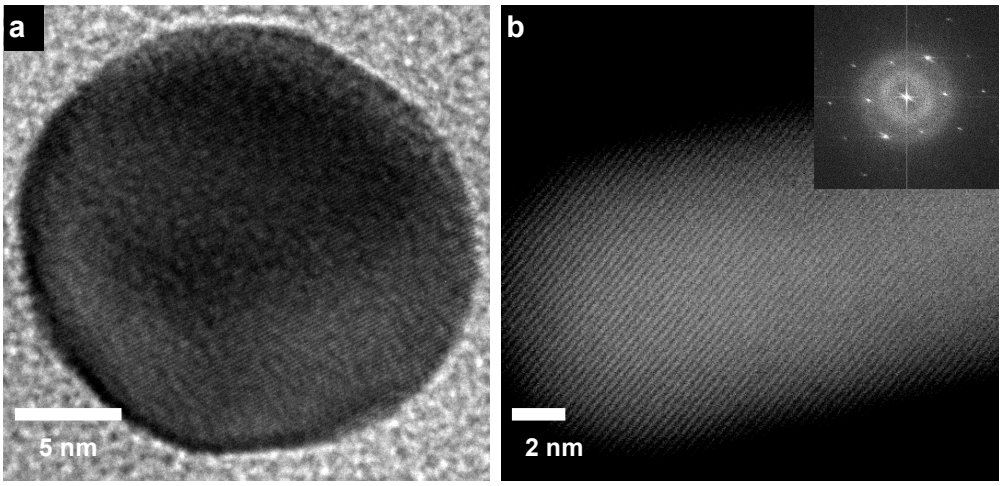

Figure 2. HRTEM images of Au seeds: (a) nanosphere (Au 2) and (b) nanorod (Au 3 – inset shows electron diffraction pattern). Scale bar: 5 nm –a and 2 nm- b.

Energy dispersive X-ray analysis (EDX) was performed on an individual Au nanorod (Figure 3) as well as the entire imaged area (data not shown) in order to qualitatively determine the nanoparticle composition. The main components of the nanorods (gold and silver) are easily identified from their corresponding x-ray lines. The presence of bromide and nitrogen, main constituents of the CTAB, was also detected with this technique for the first time in the literature. The strong copper signal results from electron scattering due to the TEM copper grid. Figure 3b shows the spot location of the beam during EDX acquisition. Inductively coupled plasma mass spectrometry (ICP-MS) was also performed for a more rigorous quantitative analysis. The results demonstrate (data not shown) that only ~15% of the nominal Au ions introduced in the reaction transformed into Au nanoparticles, which agrees with earlier reports (Orendorff et al. 2006).

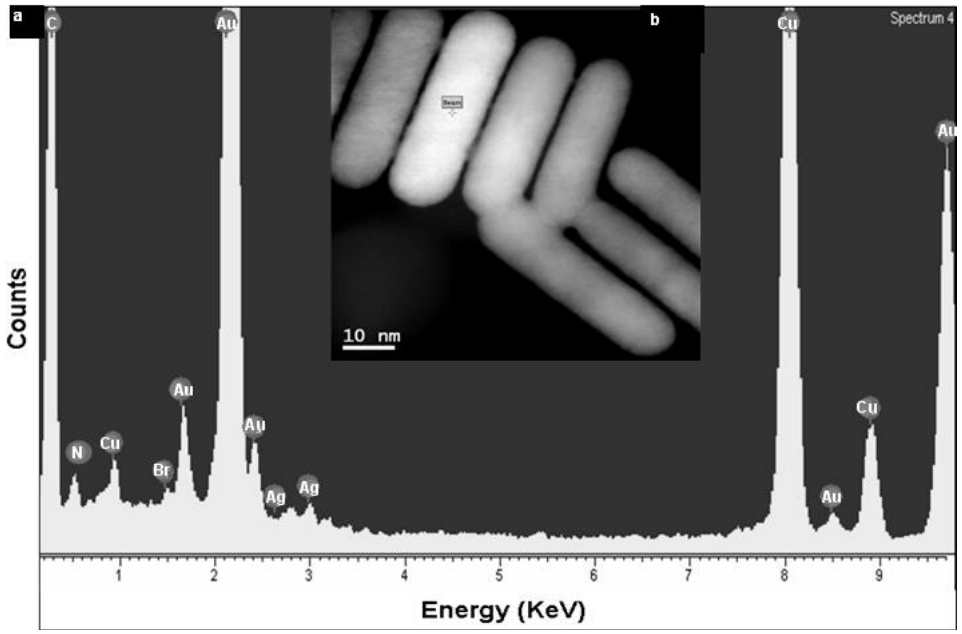

Figure 3. (a) Energy dispersive X-ray spectrum (EDAX) of an individual Au nanorod prepared in the presence of Ag ions; (b) Corresponding TEM image defining the EDX acquisition spot.

UV-Vis spectra were also used to characterize the Au nanoparticle seeds since their visible spectra will vary depending on their aspect ratios (Nehl, et al. 2008). For example, Au seeds with an aspect ratio of one display a single plasmon band (collective oscillation of electrons) with maxima around 524 nm (Table 2, Au 1). On the other hand, anisotropic nanoparticles exhibit two plasmon bands: longitudinal and transverse. This is due to the nanorods ability to absorb and scatter light along multiple axes: the long axis (longitudinal plasmon band) and the short axis (transverse plasmon band). The data shows that the longitudinal plasmon band maxima for the Au seeds increase from 575 nm to ~750 nm according to aspect ratio which agrees with our previously reported values (Hunyadi et al. 2006, 2009; Hunyadi Murph et al. 2010, 2011; Murphy et al. 2005, 2006). A representative spectrum of a Au nanorod solution (Au 5) and the corresponding Au-Pt nanocatalyst product is presented in Figure 4.

Table 2 shows the maxima of the longitudinal plasmon band for Au seeds and Au-Pt nanocatalysts. A significant red shift was recorded for all Au-Pt nanocatalysts relative to their template nanoparticles, as expected based on previous theoretical modeling studies (He et al. 2010).

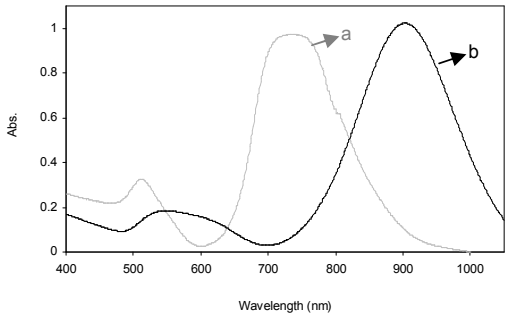

Figure 4. UV-Vis spectra of (a) Au nanorod seeds Au 5 (grey line) and (b) Au-Pt 5 dogbone nanocatalysts (black line)

Table 2. Maxima of the longitudinal plasmon band for Au seeds and Au-Pt nanocatalysts; Au 1 seed and Au-Pt 1 have a single plasmon band.

Sample	Au 'seed'	Au-Pt
1	524	533
2	578	666
3	618	800
4	658	872
5	734	911

Characterization of Au-Pt nanocatalysts

We have repeatedly demonstrated the synthesis of well defined metallic nanoparticles of different size, shape and compositions by a seed-mediated growth approach (Sau et al. 2004; Murphy et al. 2005, 2006; Hunyadi Murph et al. 2010, 2011; Hunyadi et al. 2006, 2009). This procedure is a simple and straightforward route that provides uniform nucleation templates or 'seeds' with predetermined size, geometry and composition which can be further grown in a homogeneous or heterogeneous epitaxial fashion (Figure 5). Novel nanomaterials with unique morphologies can be produced by simply controlling experimental conditions such as reaction temperature, time, and the concentrations of the metal ions, capping reagents, and reducing agents. These conditions include reaction temperature, time, and the concentrations of solvent, capping reagents, and reducing agents. (Murphy et al. 2005, 2006; Hunyadi Murph et al. 2010, 2011; Hunyadi et al. 2006, 2009). The resulting monometallic or bimetallic nanostructures display novel electronic, optical and catalytic properties distinct from their template nanoparticles.

Au–Pt nanocatalysts of various size, shape and aspect ratios were synthesized by our seed-mediated approach. The previously discussed Au nanoparticles of varying aspect ratio (Au 1-Au 5) were used as seeds in reactions with identical concentrations of a platinum salt and a weak reducing agent. CTAB was used as a surfactant and stabilizer of the nanocatalysts. The resulting particle morphologies included cubes, blocks, octahedrons and dogbone shapes of various aspect

ratios. For easier reading, the particles have been identified as Au-Pt 1 to Au-Pt 5, according to increasing aspect ratio (Table 1).

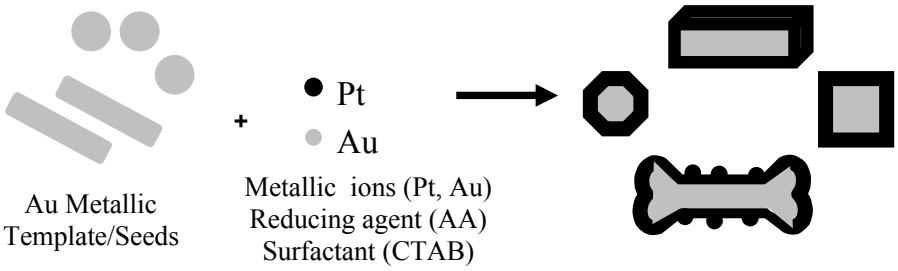

Figure 5. Seed mediated synthesis procedure for the synthesis of bimetallic Au-Pt nanocatalysts with controlled morphologies: Au-grey and Pt-black.

TEM images (Figure 6 and SI-Figure 1) were used to characterize the morphology and dimensions of the synthesized Au-Pt nanocatalysts (Table 1). As expected, variations in the Au seed morphology, from spheres to nanorods, altered the final shape of the synthesized Au-Pt nanocatalyst product, resulting in novel nanostructures. Monodisperse and uniform octahedrons, blocks and dogbones of various aspect ratios (2.9, 3.1, and 3.5) were produced in high yield, ~73%, ~80% and ~94-97%, respectively (Figure 6 and SI-Figure 1). The length and diameter of the Au-Pt nanocatalysts increased ~5-30%, while their aspect ratio decreased when compared to their template seeds (Table 1). For instance, Au-Pt dogbones of aspect ratio of 3.5 where grown from Au nanorod seeds with an aspect ratio of 4.2.

As expected, a strong correlation was found between the initial Au seed morphology and the resulting Au-Pt nanocatalyst structure. For instance, octahedron or cubic Au-Pt nanocatalysts were produced from Au spherical seeds. As the aspect ratio of the original Au seed increased to ~2-3, anisotropic structures (blocks and dogbones) were produced.

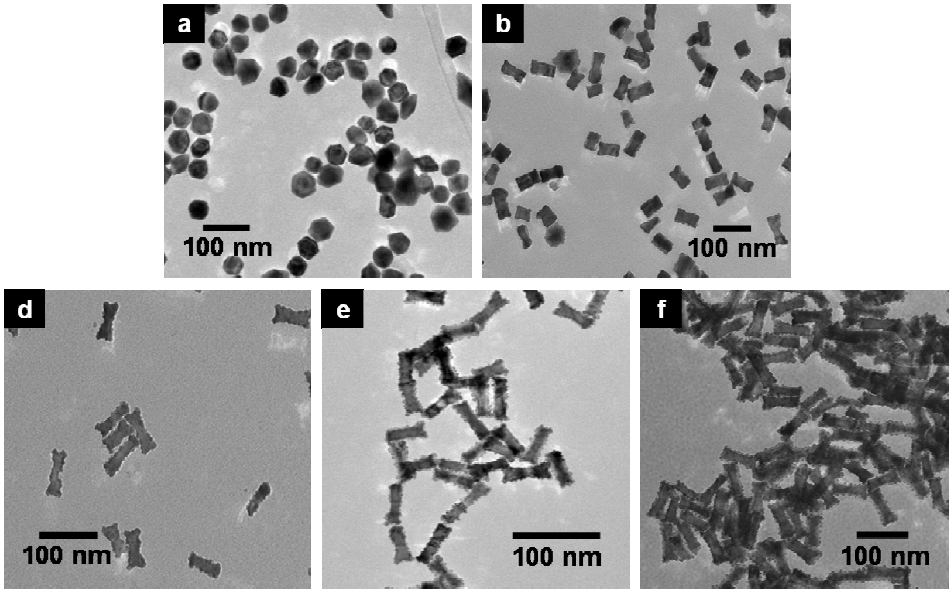

Figure 6. Au-Pt nanocatalysts with various morphologies and aspect ratio (a) Au-Pt 1 octahedrons, (b) Au-Pt 2 blocks and cubes, (c) Au-Pt 3 dogbones, (d) Au-Pt 4 dogbones, (e) Au-Pt 5 dogbones. Scale bars: 100 nm a-e.

TEM images (Figure 5 and SI-Figure 1) also revealed interesting variations of surface morphology across the different Au-Pt nanocatalysts. Close inspection shows that the geometry and surface area of the seed template plays a critical role in the final nanocatalyst morphology. For instance, Au-Pt octahedrons with uniform and smooth surfaces were produced from Au spheres, while Au-Pt dogbones with nanoisland-like protuberances arise from the Au nanorod templates. The nano-island sizes decrease from ~6 to ~4 nm as the aspect ratio of the Au-Pt nanocatalyst increased from ~2.9 to ~3.5 (SI-Table 2). These protrusions and non-uniformities can be controlled

by adding more than one-monolayer equivalent of Pt ions per given Au seed surface area. This finding warrants further investigation since the presence and control of these protrusions is of particular interest for catalytic applications due to the additional active surface area that they provide (Roucouxet al 2002).

Atomic force microscopy (AFM) analysis was used to characterize the morphology of the Au-Pt nanocatalysts as drop-casted on Si wafers (SI-Figure 2). Line scans were measured across the width and length of the dogbone shaped nanocatalysts, resulting in dimensions of ~81 and ~25 nm. These results match closely those from TEM measurements. Since the Au-Pt nanocatalysts were not chemically attached to the Si wafer, the shape resolution is slightly hindered by particle drifting due to tip interaction. The issue has been previously reported in the literature (Rao et al 2007).

X-Ray energy dispersive microanalysis (EDX) was performed to qualitatively elucidate the bulk composition of the bimetallic Au-Pt nanocatalysts (SI-Figure 2). The results reveal the presence of the main elements constituents, Au and Pt. No significant signals from the Ag additive ions and the CTAB surfactant (N, Br) were observed due to low instrument surface resolution.

A surface analytical technique (<10 nm), X-ray photoelectron spectroscopy (XPS), was used to accurately elucidate the composition and uniformity of the Au-Pt nanocatalysts based on the binding energy of the core electrons (Figure 7). XPS analysis on the Au nanoparticle seeds was used for comparison (Figure 8). Figure 7 shows the high resolution scans of sample Au-Pt 3, which indicates the presence of Pt, Au, Ag, and Br (from the CTAB surfactant). In the case of Pt, Au and Ag, further inspection of the spectra shows closely-spaced double photoemission peaks. These doublets arise from spin-orbit coupling effects of the metallic Pt, Au and Ag. The peak assignments are in agreement with data reported elsewhere (Turner et al. 1990; Thomas et al. 1986). By comparison, high resolution scans of the Au nanorod seeds (Au 3) revealed similar results. The position of the Au 4f and Pt 4f lines indicate that both Au and Pt are metallic. The presence of the Br 3d line indicates that the CTAB counterions are adsorbed on the surface of both the Au nanorod seeds and the Au-Pt dogbone nanocatalysts. To further understand the state of the Ag and whether it is bonded to Br, the Ag MNN auger lines were scanned since these are more sensitive to bonding changes than the Ag 3d lines. The Ag $M_4N_5N_5$ Auger transitions are consistent with metallic Ag in both Au and Au-Pt samples. XPS survey spectra shows an increase in the high binding energy background for both the Au 4f and Pt 4f lines of sample Au-Pt 3, which is caused by the scattering of exiting photoelectrons.

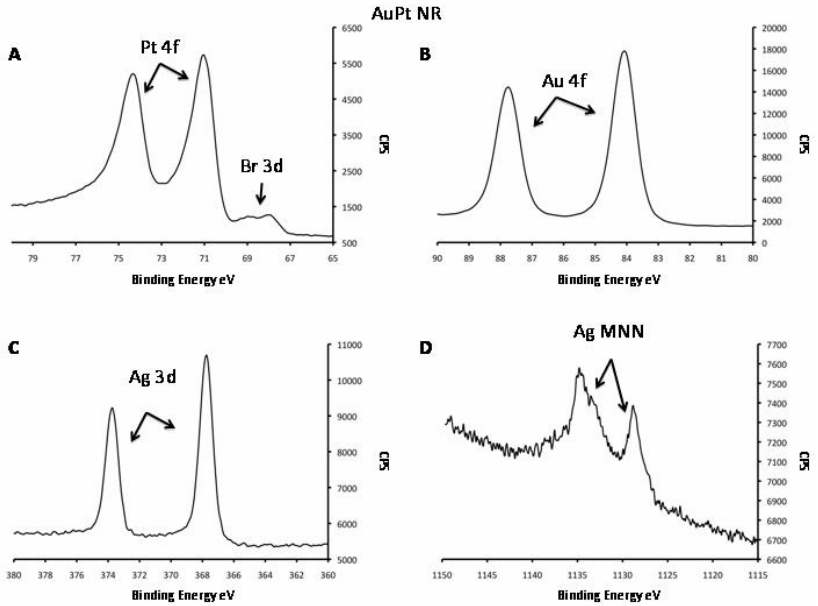

Figure 7. XPS and Auger analysis of the Au-Pt nanocatalysts: Pt (A), Au (B), Ag (C) and Ag MNN (D) regions. The increase in the high energy background indicates that the element resides at depths greater than 10 nm.

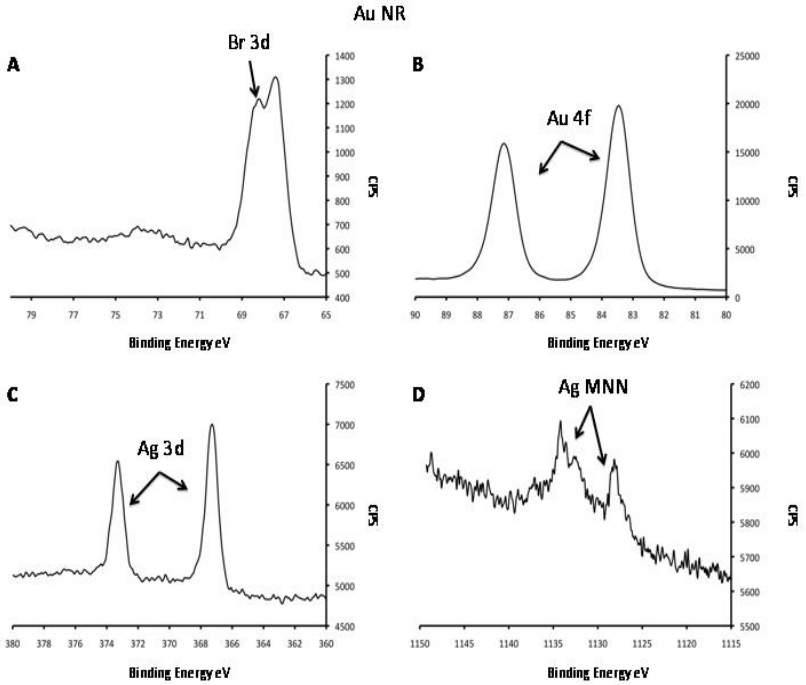

Figure 8. XPS and Auger analysis of Au nanorod 'seeds': Br (A), Au (B), Ag (C) and Ag MNN (D) regions

Inductively coupled plasma mass spectrometry was also performed on the Au-Pt nanocatalysts for accurate bulk compositional analysis (SI-Table 3). ICP-MS results indicate that the nanocatalysts show homogeneous surfaces at concentrations of [Pt]/[Au] ≤ 0.11, while discrete Pt nanoislands and protrusions are produced at concentrations ≥ 0.14. These concentrations were further used for calculations of the surface area in the electrochemical studies.

Platinum deposition and growth on the Au nanoparticle templates can be easily monitored by UV–Vis–NIR spectrophotometry. Figure 9 shows the optical absorption spectra of the Au-Pt nanocatalysts with varying aspect ratio. The transverse plasmon band maximum in the visible region ranges from ~530 to 550 nm and from ~700 to 930 nm for the longitudinal plasmon band

All Au nanoparticles seeds showed a significant red shift of the surface plasmon bands after Pt deposition, as presented in Figure 4 and Table 2. Figure 3a and Table 2 shows images of DI water dispersions of the as-prepared nanoparticle seeds Au 5 (L=76±3nm; d=19±2nm) and the resulting dogbone-shaped nanocatalysts Au-Pt 5 (d=83±3nm nm and L=24±2nm. In the absence of the Pt shell, the Au nanorods display blue color absorption due to their two characteristic transverse and longitudinal plasmon absorption bands at 520 and 630 nm, respectively. Following Pt deposition, the color of the dispersion changes from blue to grey.

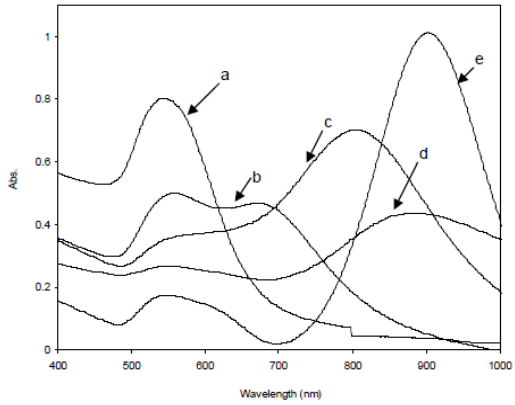

Figure 9. UV-Vis spectra of Au-Pt nanocatalysts : (a) Au-Pt 1, (b) Au-Pt 2 , (c) Au-Pt 3, (d) Au-Pt 4, (e) Au-Pt 5. The aspect ratio varies from (a) 1.1, (b) 1.7, (c) 2.9, (d) 3.1, (e) 3.5.

Figure 10 shows images of dispersions containing the Au seed nanoparticle seeds (top row) and the corresponding reaction product Au-Pt nanocatalysts (bottom row). A gradual change of color was observed according to the increasing aspect ratiodue to the shifts in the transverse and longitudinal plasmon bands.

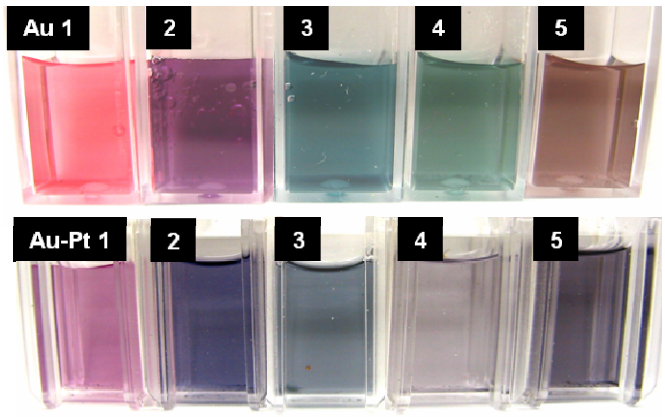

Figure 10. Aqueous dispersions of Au nanoparticle seeds (top row) and the product Au-Pt nanocatalysts (bottom row). The aspect ratio increases from left to right.

Zeta potential measurements are an excellent tool for measuring changes in the nature of the shell around the Au seed nanoparticles in solution. The Au seeds prepared by the silver assisted mediated approach are stabilized by the CTAB bilayer and have an effective surface charge of ~+30mV as determined by zeta potential experiments (Figure 11-grey). This is due to the positively charged quaternary nitrogen of the CTAB surfactant, as demonstrated earlier by the FTIR and thermogravimetric studies (Murphy et al. 2005, Murphy et al. 2006). Our previous studies showed the importance of the CTAB surfactant, including concentration and placement on the Au nanorod surface. After Pt deposition the surface charge analysis shows an average of ~+15 mV (Figure 11-black), which implies that some of the CTAB bilayer is removed or rearranged on the surface (Gou et al 2005). This is certainly possible, since the synthesis procedures of Au-Pt nanocatalysts takes place at slightly elevated temperatures. During the heating process, the CTAB bilayer is more likely to be destabilized and no longer tightly packed on the nanorod long-axis surface. In addition, CTAB with Br^- counter ions might have a lower affinity for Pt (Mangussen 2002) or some other anionic Pt species are associated with the nanocatalysts.

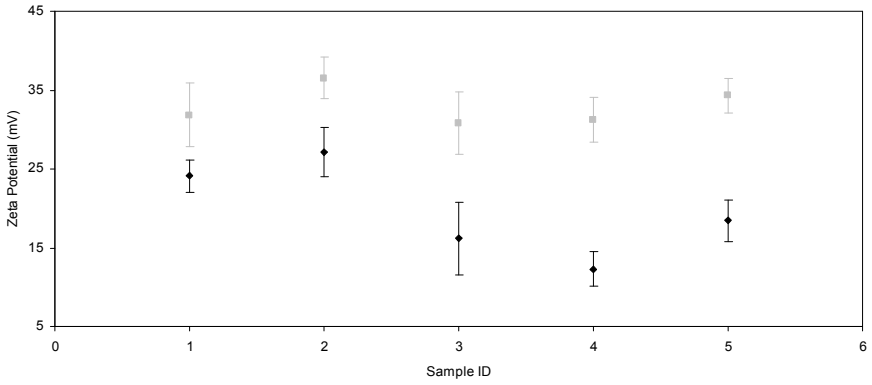

Figure 11. Zeta potential measurements recorded on Au nanoparticle seeds (grey) and Au-Pt nanocatalysts (black). The aspect ratio increases from left to right.

Insights into growth mechanism of Au-Pt nanocatalysts

According to heterogeneous nucleation and growth theory, the predominant growth mode of Pt onto a template will be primarily determined by the lattice mismatch, as well as differences in bond strength and electronegativity relative to the gold support (Bauer et al. 1986; Fan et al. 2008). Epitaxial Pt overgrowth can occur by three possible modes: (a) layered growth (Frank-van der Merwe mode), (b) island growth (Volmer-Weber mode) and (c) intermediate or combined growth (Stranski-Krastanow mode).

Figure 12a shows a HRTEM image of the Au-Pt octahedron (Au-Pt 1) nanocatalysts. The image displays well-defined and continuous {111} fringes (d ~ 0.236 nm), which extend at a ~45° angle from Pt facet overgrowth. The uninterrupted extension of the fringes across the core-shell interface suggests an epitaxial layered Pt growth mode on the spherical Au seeds. That is, the smaller Pt atoms (radius: 139 pm) can deposit on the Au core (radius: 144 pm) by uniformly releasing the lattice strain due to the minimal mismatch (Falicov, et al. 1985; Fan, et al. 2008)Figure 12b shows a HRTEM image of the Au-Pt 'dogbone'-shaped (Au-Pt 5) nanocatalysts which indicate a Stranski-Krastanow or a combined growth mode. Although an epitaxial Pt/Au shell can be observed throughout the entire Au nanorod seeds, protrusions or nanoislands preferentially form at the endcaps and end-facet corners of the rod. These protrusions which range in size of 3 to 6 nm could also incorporate not only Pt but also excess Au since the template seeds were used unpurified. The lattice arrangement of the dogbones matches that of the Au nanorod seeds (Figure 4b) due to the minimal mismatch (~ 4%), as evidenced by the continuous {002} fringes extending from the template. In lattice-matched systems like the Au-Pt bimetallic structures, nanoisland formation is driven by a high interface energy ($\gamma_{Au\text{-}Pt}$) and high epilayer surface energy (σ_{Pt}) (Eaglesham et al 1990). Nanoslands will form provided $\sigma_{Pt} + \gamma_{Au\text{-}Pt} < \sigma_{Au}$, the substrate energy, particularly at the intersection on the nanorod facets, where σ_{Au} should be the highest.

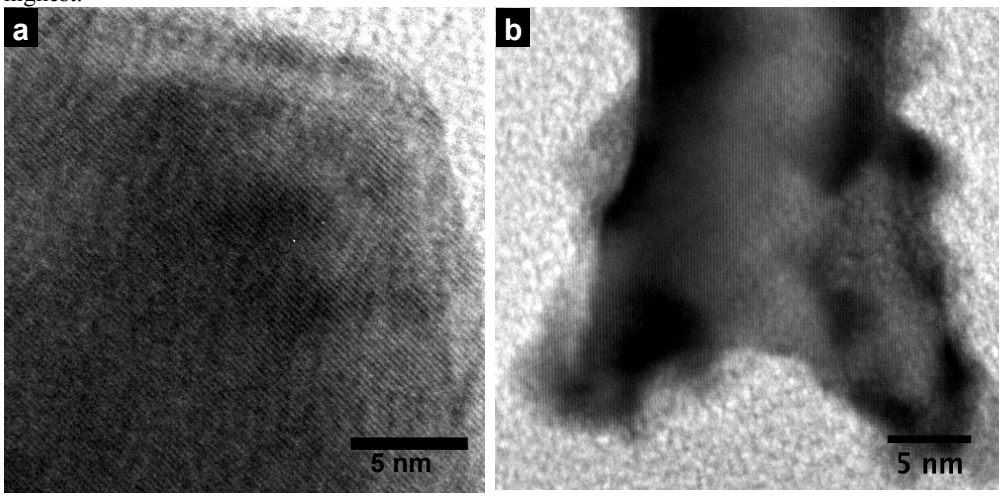

Figure 12. HRTEM images of Au-Pt nanocatalysts: (a) octahedron (Au-Pt 5) and (b) 'dogbone' shaped (Au-Pt 5).

To provide some insight into the preferential Au-Pt deposition at the Au nanorod seed endcaps, we examine the roles of the Ag^+ ions and the surfactant (CTAB) in the dogbone growth reaction. Previous studies have provided insight on the role of Ag^+ ions in the growth of Au nanorods by examining the Ag(I) underpotential deposition mechanism (Liu et al. 2005; Grzelczak et al. 2007; Orendorff et al. 2006; Rojas et al. 2000). Through this mechanism Ag^+ is reduced to metallic Ag at the gold rod surface with a lower surface potential than the bulk reduction potential of Ag^+ (Grzelczak et al. 2007). These studies showed that a larger positive shift in the Ag^+ UPD was observed for Au {110} and the {100} facets compared to the {111} surface (Rojas et al. 2000). That is, Ag deposition preferentially occurs at the sides of the Au nanorod instead of its endcaps, which have lower surface energy facets (Grzelczak et al. 2007; Carbo-Argibay et al. 2010). As a result, the Au growth rate increases from the higher energy lateral facets {100} and {110} to the close-packed plane of the fcc lattice {111}, resulting in higher Au-Pt deposition at the rod edcaps (Grzelczak et al. 2007). As mentioned earlier, recent reports by the Liz-Marzan and Etheridge groups have provided new evidence for alternate descriptions of the lateral facets in single-crystalline Au nanorods, i.e. eight-identical higher index {250} and {0 5 12} faces, respectively (Carbo-Argibay et al. 2010; Katz-Boon et al. 2011). Even with these results, the Ag(I)

underpotential should remain higher for the sides of the nanorods, as both of these new descriptions result in even higher surface energy facets. Therefore, Au-Pt deposition should continue to predominate at the endcaps of the rods, resulting in these novel dogbone-shaped Au-Pt nanocatalysts,

Recent reports have also shown the affinity of the CTAB surfactant will vary across the different facets of the Au nanorods (Murphy et al. 2005; Sajanlal et al 2010). Strongly adsorbed bromide ions induce an adlayer of positive charged surfactant on the gold surface, i.e. protonized cetyltrimethlyammonium (CTA^+) (Ha et al. 2007; Zhang et al. 2009). FTIR and thermogravimetric analysis also indicates that the hydrophobic tails of the surfactant interdigitate resulting in a bilayer on the rods (Murphy et al 2005). The strong and specific adsorption of Br^- on the Au {100} and {110} facets induces preferential binding of the CTA^+ bilayer on the sides of the nanorod seeds. The CTA^+ molecules adsorb more firmly to these facets as they have larger interatomic distances than the close-packed {111} plane of the fcc lattice (Sajanlal et al 2010; Wang et al. 2000). As the lateral surfaces of the rods are well-protected by a densely packed CTA^+ bilayer, the transfer of platinum ions to the Au side surface is limited. On the other hand, this layer is not as densely packed at the curved endcaps of the nanorods due to the high orientation freedom of the CTA^+ chain (Zhang et al. 2009). The results from the HRTEM characterization and the combination of these Ag^+ and surfactant-induced effects supports the conclusion that the Au nanorod seeds exhibit higher reactivity at their curved end facets and corners.

Electrochemical studies

The Au-Pt nanocatalysts developed herein were tested for their activity in a DMFC. The anode, cathode, and overall cell reaction for DMFC, respectively, are:

$$CH_3OH + H_2O \rightarrow 6H^+ + 6e^- + CO_2 \text{ (Eq.1)}$$

$$3/2\ O_2 + 6H^+ + 6e^- \rightarrow 3\ H_2O \text{ (Eq. 2)}$$

$$CH_3OH + 3/2\ O_2 \rightarrow 2H_2O + CO_2 \text{ (Eq.3)}$$

The anode reaction is referred to as the Methanol Oxidation Reaction (MOR) and the cathode reaction is referred to as the Oxygen Reduction Reaction (ORR), where the rate limiting step is the electrooxidation of CO at the anode. While the MOR is preferential at the anode, it can also occur at the cathode due to methanol crossover through the electrolyte, which causes a parasitic loss of power. Therefore, it is necessary to develop cathode catalyst that preferentially complete the ORR and have limited activity for the MOR.

Electrochemical measurements were performed to evaluate electronic and geometric effects on the electrochemical profile of the prepared nanocatalysts on the ORR with and without MeOH. Figure 12a shows the stable cyclic voltammograms (CVs) for sample Au-Pt 5 dogbone in 0.5 M H_2SO_4 solution tested between two potential windows. In the potential window typical for fuel cell electrocatalyst characterization and operation (-100 mV to 1200 mV) the peaks corresponding to hydrogen adsorption-desorption or hydrogen under-potential deposition (H_{UPD}) region (between -100 mV to 200 mV) and the Pt oxidation-reduction peaks (between 300 mV and 700 mV) can be observed. The H_{UPD} peaks seems to be unaffected by the inclusion of gold in the nanocatalysts with the exception of a slight shift (~50 mV) to more cathodic potentials indicating a lower adsorption energy of hydrogen at the Pt particles (Kongkanand et al. 2005).

On the other hand, the peaks corresponding to the Pt oxidation-reduction shift from a typical potential region of 650 mV to 500 mV. The Pt redox peak shift has been previously attributed to stronger Pt-O binding energies in Au rich alloys. O and OH species tend to adsorb more strongly and stabilize on the surface when the Pt-Pt distance is expanded due to the lattice increase as the Au content increases (Irissou et al. 2010). The cathodic shift in Pt oxidation potential suggests the Au-Pt electrocatalysts will be less active for the ORR when compared to a pure Pt electrocatalyst due to the higher energy that will be needed to break and desorb the O and OH species. Because this behavior is observed in the studied nanocatalysts, it is very likely the surface of the nanostructures is composed of nanoparticles rich in Pt deposited on Au rods instead of pure Pt nanoparticles deposited on Au rods. This is also supported by the XPS data shown in Figure 7, which suggests that the Pt found on the nanoparticles surface is in the higher oxidation state. Figure 13a also shows the CVs using the extended potential window (-100 mV to 1450 mV). As it can be observed from the figure, in addition to the previously observed peaks a cathodic peak at 1050 mV is observed. This peak is attributed to the gold oxide reduction most likely arising from the uncovered Au rod surface, although it is possible to observed similar peaks from Pt rich Au-Pt alloys (Möller et al. 2004).

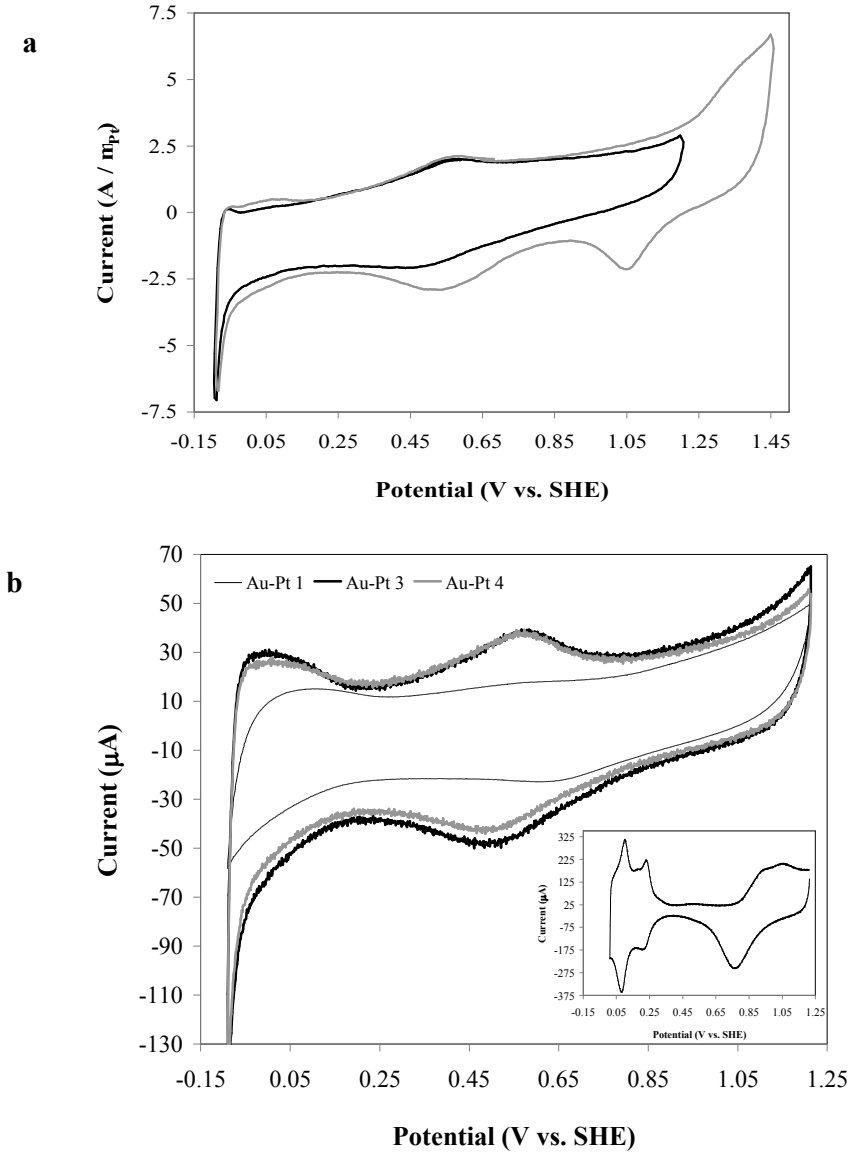

Figure 13. (a) Sample Au-Pt 5 dogbone cyclic voltammetric profile (50 mVs^{-1}) between -100 mV and 1450 mV (gray line) and between -100 mV and 1200mV (black line) in Ar-saturated 0.5 M H_2SO_4. (b) Representative cyclic voltammetric profiles (100 mVs^{-1}) between -100 mV and 1200mV in Ar-saturated 0.5 M H_2SO_4. Insert shows the cyclic voltammetry of commercial Pt black.

Because of the possible reconstruction of the nanocatalysts due to Pt dissolution/reprecipitation as a result of potential cycling, from this point forward the electrochemical studies were limited to potentials no greater than 1200 mV (Darling et al. 2005). Figure 13b shows the typical voltammograms for three different representative Au-Pt samples. The insert show the cyclic voltammetry of commercial Pt-black. As observed before, for most of the samples the two main redox peaks are observed as in the previous figure (Figure 13a). In the case of sample Au-Pt 1, with an aspect ratio of 1.1, the catalyst consists of a hexagonal geometry and no visible individual nanoparticles on the surface. Even though Au is present in the catalyst (Pt/Au: 0.11 weight ratio), no Au effects on the peak position are observed. The peaks positioning resemble those of pure Pt as it can be observed comparing it with Pt black. Sample Au-Pt 3 consists of the dogbone geometry with a similar Pt/Au weight ratio, 0.25 and 0.20 respectively. While individual discrete nanoparticles are observed in the HRTEM micrograph, the CVs do not reflect different behavior. In the case of Au-Pt dogbone samples (Au-Pt 3-5) of various aspect ratio, 2.9, 3.1 and 3.5, (only sample Au-Pt 3 and 4 shown for clarity) the Pt oxidation/reduction peak and the H_{UPD} peak are observed with the typical cathodic shift in potential (Figure 13). The

H_{UPD} is indicative of active electrochemical surface area associated with the hydrogen oxidation reaction or the oxygen reduction reaction (ORR) where surface Pt accessible for the reactions.

The activity of the nanocatalysts for the oxygen reduction reaction (ORR) was measured using rotating disk electrode. The obtained data was used to construct mass-transfer corrected Tafel plots, where the kinetic current was calculated following the relation described by Paulus et al. (Paulus et al. 2001). Figure 14a shows the Tafel plots as a function of current density evaluated using the Pt active surface area in the sample. The Pt electrochemical active surface area was obtained by using the calculated charge from the integration of the area under the H_{UPD} from the CVs and assuming a polycrystalline Pt surface area (210 μCcm^{-2}) (Toda et al. 1999). At low current densities, it is evident from the Tafel plot that sample Au-Pt 1 hexagons show the highest performance. This result can be expected as the CV shows Pt like surface; however the fact that the performance is higher than that of commercial platinum black indicates an improvement due to either shape of the nanoparticles and the fact that the particles are much larger. The activity of the other samples was reduced by 100 mV. As the plot transition to the high current density region, the Tafel slope changes indicating a change in the adsorption of reaction intermediates or a change in the surface coverage of OH which affects the adsorption of oxygen (Sarapuu et al. 2008).

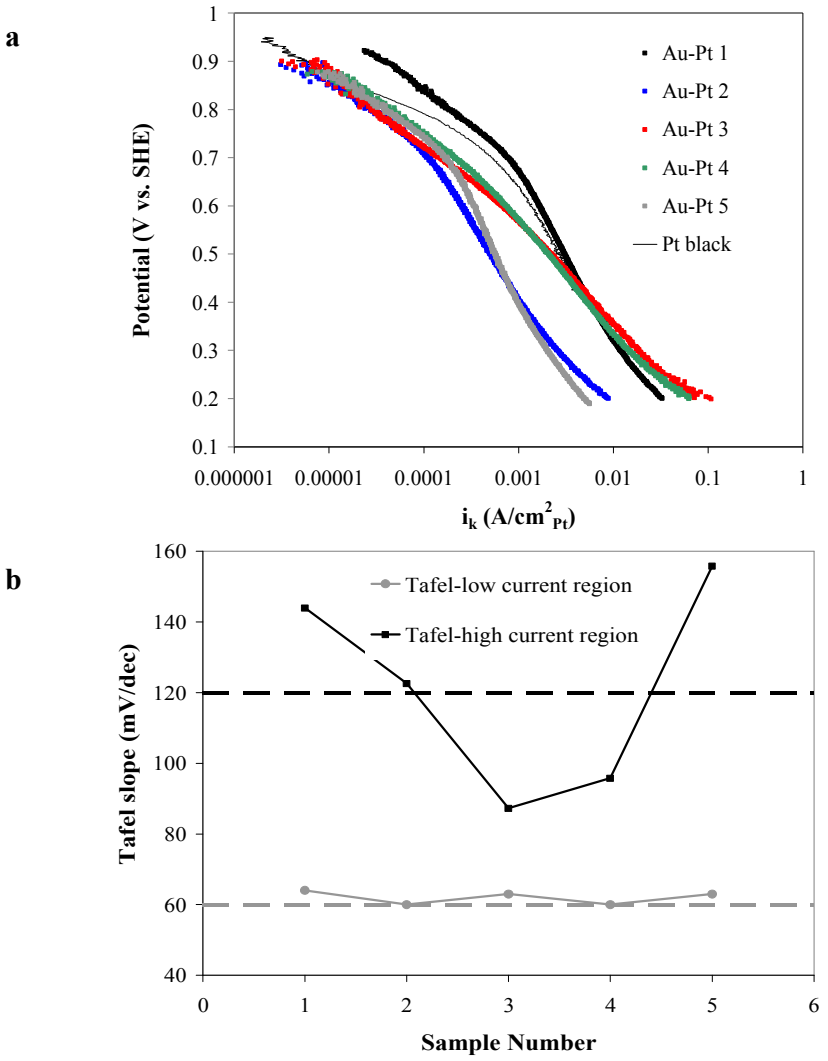

Figure 14. (a) Mass transport corrected Tafel plots for O_2 reduction on the different Au-Pt nanocatalysts in O_2 saturated 0.5 M H_2SO_4. Current density evaluated using Pt electrochemical active surface area from the CVs. Sweep rate 10 mVs^{-1} and a rotation rate 800 rpm. (b) Mass transport corrected Tafel slopes for O_2 reduction on the different Au-Pt nanocatalysts. Conditions same as in (a).

Typical Pt samples show two slopes, one slope of ca. -60 mV/dec at low current density and a slope of ca. -120 mV/dec at high current density. The change in slope is a reflection of the potential dependent oxide coverage on the Pt surface (Kongkanand et al 2005). Figure 14b shows the low and high current density Tafel slopes for samples tested. The low current density slopes of all the samples tested are in accordance with the values typically observed for Pt samples. However the high current region of samples Au-Pt 3 and Au-Pt 4 show values at ~ 90 mV/dec. similar to behavior observed by Kongkanand et al. This behavior can be explained by Irissou, et al. that shows Pt oxides formed at Au-rich alloys are more difficult to reduce compared to Pt-rich alloy surfaces, consistent with the cathodic shift observed in the CVs. As the oxophilicity increases, the formation of OH species that are known to be responsible for blocking the O_2 adsorption sites results in lower ORR activity by most Au-Pt alloys (Irissou et al. 2010).

To test the effects of a more oxophilic Pt surface, the catalyst performance was investigated for the methanol oxidation reaction (MOR). Figure 15a shows the typical voltammograms for three different samples in the presence of 0.1 M methanol. As observed before, the typical Pt signature peaks are observed with the addition of the peak for MOR. Sample Au-Pt 1 (hexagons) shows the highest catalytic activity for the MeOH oxidation followed by the dogbone geometry (sample Au-Pt 3, the smallest aspect ratio dogbone). While all the samples tested show activity for MOR, the dogbones show reduced oxidation currents for the MOR as compared to sample Au-Pt 1-hexagons. The hexagon-shaped nanocatalysts do not have discrete Pt islands that were detectable by TEM, as was the case for the dogbones (see Figure 12). This may indicate that the Pt particle size and surface irregularities may have a significant impact on the catalyst activity and might warrant further investigation.

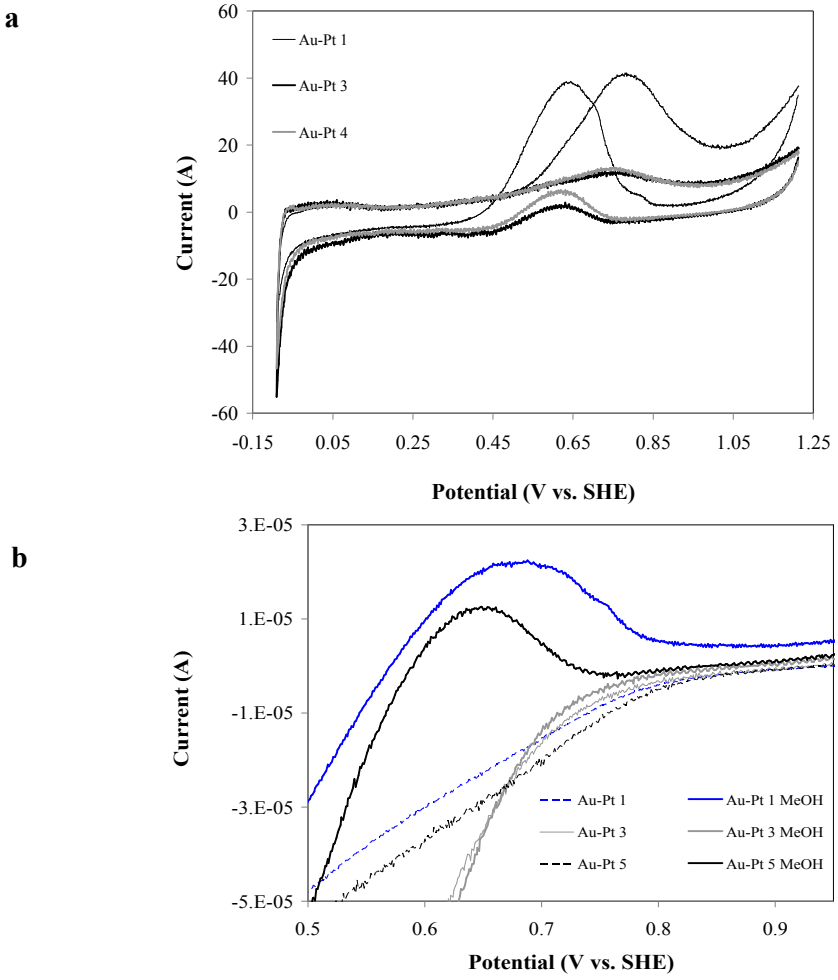

Figure 15. (a) Representative cyclic voltammetric profiles (100 mVs^{-1}) between -100 mV and 1200mV in Ar-saturated 0.5 M H_2SO_4 and 0.1 M MeOH; (b) Linear sweep voltammetry on the different Au-Pt nanocatalysts in O_2 saturated 0.5 M H_2SO_4 with and without 0.1 M MeOH. Current density evaluated using Pt electrochemical active surface area from the CVs. Sweep rate 10 mVs^{-1} and a rotation rate 800 rpm.

The effects observed in the high current region of the Tafel slope are clearer in the ORR evaluation in the presence of MeOH. While MeOH is not usually in the cathode side, the un-reacted methanol from the anode tends to cross to the cathode through the proton conducting membrane. Typically the presence of methanol in the cathode electrode reduces the performance of the electrode for the ORR by adding the competing reaction of the MOR. A solution for this behavior is to use highly selective electrocatalysts for the ORR and non-selective catalysts for the MOR. The presence of catalysts with stronger bonding affinity for oxygen species results in a catalyst surface where the sites for methanol oxidation will have to compete for it to be adsorbed and react. Figure 15b shows the effects of adding MeOH in the O_2 saturated electrolyte solution. As can be observed, samples with high Tafel slopes (>100 mV/dec) shows the effects of MeOH, while sample Au-Pt 3 shows no effects with the addition of MeOH.

The implication of the synthesis of a Pt electrode that shows no activity in the presence of O_2 is of great value for direct methanol fuel cells cathode catalysts. The fact that the Au-Pt dogbone with low Tafel slope at the high current region (such as samples Au-Pt 3 and 4) that are less prone to the MeOH oxidation can also indicate a new generation of anode electrocatalysts less prone to CO poisoning, as CO is one of the decomposition products in the indirect pathway to produce CO_2 from MeOH (Lai et al. 2007). This indicates that the electrochemical activity of the nanocatalysts can be tailored for specific reactions based on nanocatalysts shape, particle size and surface irregularities. In this case, the dogbones would be useful preferentially at the cathode where they demonstrate high activity for the ORR, but reduced activity for the MOR. The hexagon shaped nanoparticles would be preferential at the anode, where they have high selectivity for the MOR.

Conclusions

In summary, we have produced and proposed a growth mechanism involved in the seed-mediated synthesis of Au-Pt bimetallic nanoparticles. We investigated the ORR and MOR activities and demonstrated its sensitivity to the nanoscale shape of a catalyst particle. While Au in the samples seems to lower the performance for the ORR, great benefits are observed in the presence of MeOH and O_2. Depending on the geometry and the Pt/Au ratio, Pt-based catalysts can be prepared that reduce and, in some cases, eliminate the detrimental effects of methanol crossing over to the cathode.

Acknowledgements
We gratefully acknowledge the financial support of this work by Savannah River National Laboratory LDRD-DOE. We would like to thank Dr. Kimberly Roberts, Prof. Apparao Rao, Dr. Robert Lascola, Dr. Charles Chuck and staff of electron microscopy facility at Clemson for making their instrumentation available to us.

References

Antolini E, Lopes T, Gonzalez, ER (2008) An overview of platinum-based catalysts as methanol-resistant oxygen reduction materials for direct methanol fuel cells. J Alloy Compd 461:253-262.

Bauer E, van der Merwe J (1986) Structure and growth of crystalline superlattices- from monolayer to superlattice. Phys Rev B, 33: 3657-3671.

Bell A (2003) The impact of nanoscience on heterogeneous catalysis Science 299:1688-1691.

Burda C, Chen X, Narayanan R, El-Sayed M. (2005) Chemistry and properties of nanocrystals of different shapes. Chem Rev 105: 1025-1102.

Carbo-Argibay E, Rodriguez-Gonzalez B, Gomez-Grana S et al., (2010) The crystalline structure of gold nanorods revisited: Evidence for higher-index lateral facets. Angew Chem Int Ed 49:9397 –9400.

Chen C, Akashi M (1997) Synthesis, characterization, and catalytic properties of colloidal platinum nanoparticles protected by poly(N-isopropylacrylamide) Langmuir 13:6465-6472.

Chen A, Holt-Hindle P (2010) Platinum-based nanostructured materials: synthesis, properties and applications. Chem Rev 110:3767-3804.

Darling R, Meyers J. (2005) Mathematical model of platinum movement in PEM fuel cells. J Electrochem Soc 152:A242-A247.

Eaglesham DJ, Cerullo M (1990) Dislocation-free Stranski-Krastanow growth of Ge on Si (100). Phys Rev Lett 64:1943-1950.

Falicov L, Somorjai G (1985) Correlation between catalytic activity and bonding and coordination-number of atoms and molecules on transition-metal surfaces-theory and experimental evidence. Proc. Natl. Acad. Sci. USA 82: 2207-2211.
Fan F, Liu D, Wu Y et al (2008) Epitaxial growth of heterogeneous metal nanocrystal: From gold nano-octahedra to palladium and silver nanocubes. J Am Chem Soc 130: 6949-6951.
Feng L, Wu X, Ren L et al (2008)Well-Controlled Synthesis of Au@Pt Nanostructures by Gold-Nanorod-Seeded Growth. Chem Eur J 14: 9764-9771.
Gou L, Murphy C (2005) Fine-tuning the shape of gold nanorods. Chem Mater 17:3668-3672.
Grzelczak M, Perez-Juste J, de Abajo F, Liz-Marzan L. (2007) Optical properties of platinum-coated gold nanorods. J Phys Chem C, 111:6183-6188.
Guo S, Wang L, Wang Y, Fang Y, Wang E (2007) Bifunctional Au@Pt hybrid nanorods. J Colloid Interf Sci 315:363-368.
Guo S, Wang L, Dong S, Wang E (2008) A novel urchinlike gold/platinum hybrid nanocatalyst with controlled size J Phys Chem C 112:13510-13515.
Ha TH, Koo H-J, Chung BH (2007) Shape-controlled syntheses of gold nanoprisms and nanorods influenced by specific adsorption of halide ions. J Phys Chem C 111:1123-1130.
He W, Wu X, et al Xie S (2010) Formation of AgPt alloy nanoislands via chemical etching with tunable optical and catalytic properties. Langmuir 26:4443-4448.
Hunyadi S; Murphy C (2009) Synthesis and characterization of silver-platinum bimetallic nanowires and platinum nanotubes. J Cluster Sci**,** 20: 319-330.
Hunyadi S, Murphy C (2006) Bimetallic silver-gold nanowires: Fabrication and use in surface-enhanced Raman scattering J Mater Chem 16:3929 – 3935.
Hunyadi Murph SE, Torres RD (2010) Shape selective nano-catalysts: toward direct methanol fuel cells applications. NSTI-Nanotech 3:777-778.
Hunyadi Murph S, Serkiz S, Fox E et al (2011) Synthesis, Functionalization, Characterization and Application of Controlled Shape Nanoparticles in Energy Production. Book Chapter ACS Symposium Series, accepted.
Irissou E, Laplante S, Garbarino M et al. (2010) Effect of size on the electrochemical stability of Pt nanoparticles deposited on gold substrate. J Phys Chem C 114:2192-2199
Katz-Boon H, Rossouw CJ, Weyland M, Funston AM, Mulvaney P, Etheridge J (2011) Three-dimensional morphology and crystallography of gold nanorods. Nano Lett. 11(1):273-8
Kongkanand A, Kuwabata S (2005) Oxygen reduction at platinum monolayer islands deposited on Au(111) J Phys Chem B, 109, 23190-23195.
Lai S, Lebedeva N, Housmans T et al (2007) Mechanisms of carbon monoxide and methanol oxidation at single-crystal electrodes Top Catal 46:320-333.
Liang H, Zhang H, Hu Jet al (2004). Pt hollow nanospheres: Facile synthesis and enhanced electrocatalysts Angew. Chem. Int. Ed. 43: 1540-1543.
Lide DR CRC Handbook of Chemistry and Physics, 87th ed; Taylor and Fransic; Boca Raton, FL, 2007.
Liu M, Guyot-Sionnest P (2005) Mechanism of silver (I)-assisted growth of gold nanorods and bipyramids 109: 22192-22200.
Lu Y, Yuan J, Polzer F, Drechsler M, Preussner J (2010) In situ growth of catalytic active Au-Pt bimetallic nanorods in thermoresponsive core-shell microgels. 4:7078-7086.
Magnussen O (2002) Ordered Anion Adlayers on Metal Electrode Surfaces Chem Rev 102: 679-725.
McNicol BD, Rand DAJ, Williams KR (1999) Direct methanol-air fuel cells for road transportation. J Power Sources 83:15–31.
Möller H, Pistorius P (2004) The electrochemistry of gold-platinum alloys J. Electroanalytical Chem. 570:243-255.
Murphy C, Gole A, Hunyadi, S et al (2006) One-Dimensional colloidal gold and silver nanostructures Inorg Chem, 45: 7544-7554.
Murphy C, Sau T, et al Hunyadi S (2005) Anisotropic metal nanoparticles: Synthesis, assembly, and optical applications" J Phys Chem B109:13857-13870.
Narayanan R, El-Sayed M (2005) Catalysis with transition metal nanoparticles in colloidal solution: nanoparticle shape dependence and stability, J Phys Chem B 109:12663-12676.
Narayanan R, El-Sayed M (2005) Effect of Colloidal nanocatalysis on the metallic nanoparticle shape: The Suzuki reaction. Langmuir 21:2027-2033.
Narayanan R, El-Sayed M (2003) Effect of catalytic activity on the metallic nanoparticle size distribution: Electron-transfer reaction between $Fe(CN)_6$ and thiosulfate ions catalyzed by PVP-platinum nanoparticles, J. Phys. Chem. B, 107:12416-12424.
Nehl, CL, Hafner, JH (2008) Shape-dependent plasmon resonances of gold nanoparticles. J Mater Chem 18:2415-2419.

Niidome, Y, Yuki N, Honda K et al (2009) Characterization of silver ions adsorbed on gold nanorods: surface analysis by using surface-assisted laser desorption/ionization time-of-flight mass spectrometry Chem Comm 13: 1754-1756.
Orendorff C, Murphy C (2006) Quantitation of metal content in the silver-assisted growth of gold nanorods J Phys Chem B 110: 3990-3994
Ortiz-Soto L, Alexeev O, Amiridis M (2006) Low temperature oxidation of CO over cluster-derived platinum-gold catalysts Langmuir 22: 3112-3117.
Park JY, Zhang Y, Grass M, Zhang T, Somorjai GA (2008) Tuning of catalytic CO oxidation by changing composition of Rh-Pt bimetallic nanoparticles. Nano Lett 8:673-677.
Paulus U, Schmidt T, Gasteiger H et al (2001) The oxygen reduction reaction on a Pt/carbon fuel cell catalyst in the presence of chloride anions J Electroanalytical Chem 495:134-145.
Paulus U, Endruschat U, Feldmeyer, G et al (2000) New PtRu alloy colloids as precursors for fuel cell catalysts. Journal of Catalysis 195:383-393.
Rao A, Schoenenberger M et al. (2007) J Phys Conf Ser 61: 971-976.
Ren H, Humbert MP, Menning CA, Chen JG, Shu Y, Singh UG, Cheng WC (2010) Inhibition of coking and CO poisoning of Pt catalysts by the formation of Au/Pt bimetallic surfaces. Appl Catal A Gen 375:303-309.
Rojas M, Sanchez C, Del Popolo M (2000) An embedded atom approach to underpotential deposition phenomena Surf Sci 453: 225-228.
Roucoux A, Schulz J, Patin H (2002) Reduced transition metal colloids: A novel family of reusable catalysts? Chem. Rev. 102: 3757-3778.
Sajanlal P, Pradeep T (2010) Bimetallic Mesoflowers: Region-Specific Overgrowth and Substrate Dependent Surface-Enhanced Raman Scattering at Single Particle Level Langmuir 26: 8901–8907.
Sarapuu A, Kallip A, Kasikov L et al (2008) Electroreduction of oxygen on gold-supported thin Pt films in acid solutions J. Electroanalytical Chemistry 624: 144-150.
Sau T, Murphy C (2004) Seeded High Yield Synthesis of Short Au Nanorods in Aqueous Solution Langmuir, 20: 6416-6420.
Shi A, Masel R (1989) The effects of gas-adsorption of particle shapes in supported platinum catalysts J Catal, 120: 421-431.
Somorjai GA, Blakely DW (1975) Mechanism of catalysis of hydrocarbon reactions by platinum surfaces. Nature 258, 580.
Somorjai G, Rioux R, Grunes J (2005) Fabrication of two-dimensional and three-dimensional platinum nanoclusters to serve as high technology catalysts – Catalysts Capable of 100% Reaction Selectivity, In Clusters and Nano-Assemblies Physical and Biological Systems. Eds. P. Jena, S. N. Khanna, B. K. Rao. World Scientific, Singapore, 97-127.
Thomas D, Wightman P. (1986) Valence Electronic Structure of AuZ and AuMg Alloys Derived from a New Way of Ananlyzing Auger- Parameter Shifts Phys Rev B 33:5406-5413.
Tian N, Zhou ZY, Sun SG, Ding Y, Wang ZL (2007) Synthesis of tetrahexahedral platinum nanocrystals with high-index facets and high electro-oxidation activity. Science 316:732-735.
Turner N, Single A (1990) Determination of Peak Positions and Areas from Wide Scan XPS Spectra", Surf Interf Anal 15: 215-222.
Vidal-Iglesias FJ, Solla-Gullón J, Rodríguez P, Herrero E, Montiel V, Feliu JM, Aldaz A (2004) Shape-dependent electrocatalysis: ammonia oxidation on platinum nanoparticles with preferential (1 0 0) surfaces. Electrochem. Commun. 6: 1080.
Wang Z, Mohamed M, El-Sayed M (1999) Crystallographic facets and shapes of gold nanorods of different aspect ratios. Surf Sci 440:L809-L814.
Wang ZL, Gao RP, Nikoobakht B, El-Sayed, MA (2000) Surface reconstruction of the unstable {100} surface in gold nanorods. J. Phys Chem B 104:5417-5420.
Wang S, Kristian N, Jiang S, Wang X (2008) Controlled deposition of Pt on Au nanorods and their catalytic activity towards formic acid oxidation. Electrochem Commun 10:961-964.
Williams, K.R.; Burstein, G.T. (1997) Low temperature fuel cells: Interactions between catalysts and engineering design. Catal Today 38:401-410.
Xia Y, Xiong Y, Lim B, Skrabalak SE (2009) Shape-controlled synthesis of metal nanocrystals: simple chemistry meets complex physics? Angew Chem Int Ed 48: 60– 103.
Yu YY, Chang SS, Lee CL, Wang CRC (1997) Gold nanorods: electrochemical synthesis and optical properties. J Phys Chem B 101:6661-6664.
Zeng J,Yang J, Lee JY, Zhou W (2006) Preparation of carbon-supported core-shell Au-Pt nanoparticles for methanol oxidation reaction: The promotional effect of the Au core. J Phys Chem B 110:24606-24611.

Zecchina A, Groppo E, Bordiga S. (2007) Selective catalysis and nanoscience: An inseparable pair. Chem Eur J 13:2440-2460.
Zhang J, Sasaki K, Sutter E, Adzic RR (2007) Stabilization of platinum oxygen-reduction electrocatalysts using gold clusters. Science 315:220-222.
Zhang D, Diao P, Zhang Q (2009) Potential-Induced Shape Evolution of Gold Nanoparticles Prepared on ITO Substrate J. Phys. Chem. C 113: 36-39.
Zhong C, Luo J, Fang B et al (2010) Nanostructured catalysts in fuel cells. Nanotechnology 21:062001.

Supplemental Information

Tuning of Size and Shape of Au-Pt Nanocatalyst for Direct Methanol Fuel Cells

Simona E. Hunyadi Murph,[1]* Catherine J. Murphy,[2] Hector R.Colon-Mercado,[1] Ricardo D. Torres,[1] Katie J. Heroux,[1] Elise B. Fox,[1] Lucas B. Thompson,[2] Richard T. Haasch[3]

[1]*Savannah River National Laboratory, Savannah River Site, 735-11A, Aiken, SC 29808*
[2] *Department of Chemistry, University of Illinois at Urbana-Champaign, 600 S. Mathews Ave, Urbana, IL 61801*
[3]*Frederick Seitz Materials Research Laboratory, University of Illinois at Urbana-Champaign, 302 MRL, MC-230, Urbana, IL 61801*

**To whom correspondence should be addressed*
*Simona.Murph@srnl.doe.gov , Phone #: 1-803-725-8159, Fax: 1-803-725-4478

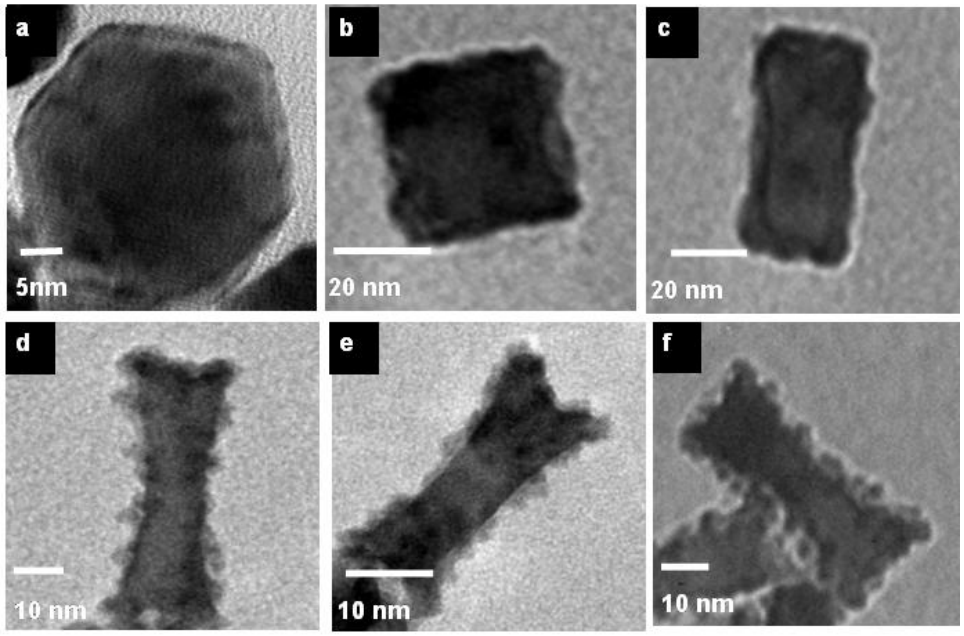

Figure 1. TEM images of individual Au-Pt nanoparticles (a) octahedron, (b) cube, (c) block, (d) – (f) different aspect ratio dogbones.

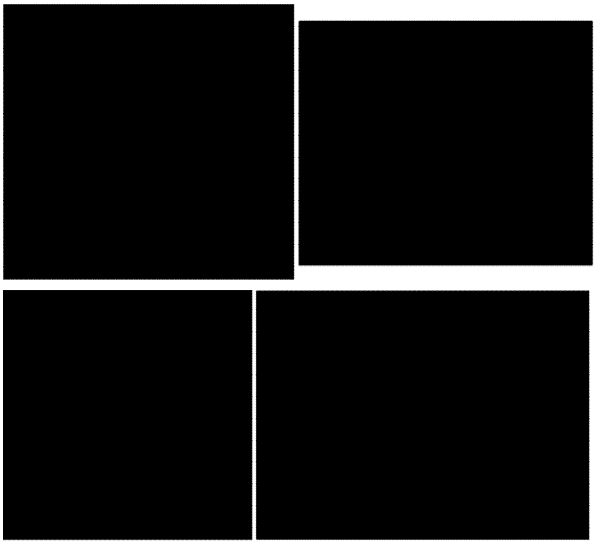

Figure 2. AFM height images of Au-Pt dogbone (Au-Pt 5-top) and octahedron-shaped (Au-Pt 1-bottom) particles drop-casted from dispersions in DI water (Si wafer substrate).

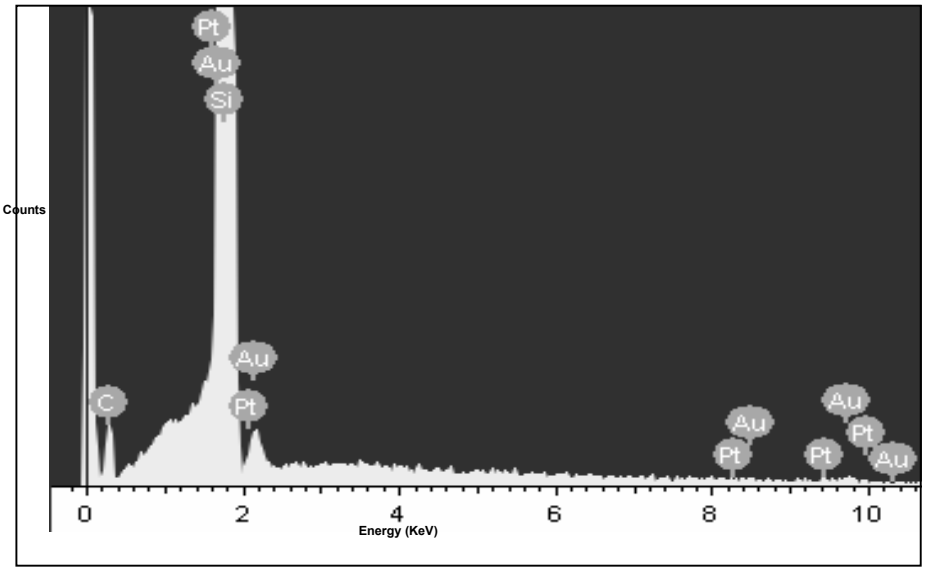

Figure 3. Energy Dispersive X-ray Analysis (EDAX) on Au-Pt 5 dogbones.

Table 1. Dimensional characteristics of Pt nano-island on the Au-Pt dogbone structures.

Sample	Pt island size (nm)
Au-Pt 3	6±1
Au-Pt 4	5±1
Au-Pt 5	4±1

Table 2. ICP-MS analysis of Au-Pt nanocatalysts of various aspect ratio.

Au-Pt substrate	[Pt], ppb	[Au], ppb	[Ag], ppb	Ratio [Pt]/[Au]
Au-Pt 1	13	120	4.1	0.11
Au-Pt 2	34	360	11	0.09
Au-Pt 3	12	59	11	0.20
Au-Pt 4	67	360	32	0.19
Au-Pt 5	82	580	37	0.14